Available online at www.sciencedirect.com
ScienceDirect
Trans. Nonferrous Met. Soc. China 32(2022) 4050−4061
Transactions of Nonferrous Metals Society of China
www.tnmsc.cn

Effects of phosphate precursors on morphology and oxygen evolution reaction activity of NiFe (oxy)hydroxide on nickel foams

Ran DUAN[1,2], Ye-jun LI[1,2], Shu WANG[1], Yong-gang TONG[3],
Horst-Günter RUBAHN[4], Gu-fei ZHANG[4], Wei-hong QI[5]

1. Hunan Key Laboratory of Nanophotonics and Devices,
School of Physics and Electronics, Central South University, Changsha 410083, China;
2. School of Materials Science and Engineering, Central South University, Changsha 410083, China;
3. College of Automotive and Mechanical Engineering,
Changsha University of Science and Technology, Changsha 410076, China;
4. NanoSYD, Mads Clausen Institute and DIAS Danish Institute for Advanced Study,
University of Southern Denmark, Alsion 2, DK-6400 Sonderborg, Denmark;
5. Center of Advanced Lubrication and Seal Materials, State Key Laboratory of Solidification Processing,
Northwestern Polytechnical University, Xi'an 710072, China

Received 24 September 2021; accepted 24 January 2022

Abstract: NiFe (oxy)hydroxides nanosheets were synthesized on nickel foams via co-precipitation and electrochemical activation. It is found that the phosphate precursors (Na_3PO_4, Na_2HPO_4 and NaH_2PO_4) have diverse effects on the morphology and thus the oxygen evolution reaction activity of the formed final catalysts. The resulting NiFe (oxy)hydroxides nanosheets prepared with Na_2HPO_4 demonstrate a low overpotential of 205 mV to achieve a current density of 50 mA/cm^2 with a Tafel slope down to 30 mV/dec in 1 mol/L KOH, and remain stable for 20 h during stability test.
Key words: NiFe (oxy)hydroxides; Fe-based phosphate; oxygen evolution reaction; electrochemical activation

1 Introduction

Electrochemical water splitting provides a sustainable and pollution-free method for mass production of high-purity hydrogen fuel [1−4]. In contrast to the rather straightforward hydrogen evolution reaction (HER) with a relatively low overpotential, the oxygen evolution reaction (OER) involves a complex four-electron transfer process with a large overpotential, which limits the overall efficiency of water electrolysis [5,6]. Noble metal compounds such as RuO_2 and IrO_2 have been used as commercial OER catalysts, while the scarcity and high cost of noble metal compounds hinder the industrial applications [7−9]. Accordingly, research efforts are increasingly devoted to the design and fabrication of energy-efficient noble-metal-free catalysts, e.g., transition metal-based oxides [10,11], phosphides [12], (oxy)hydroxide [12,13], and phosphates [14].

Among them, transition metal (oxy)hydroxides have been reported to be promising candidates for OER electrocatalysts due to the low-cost, earth abundant, environmentally benign, unique atomic geometry structure, and high catalytic behavior [15−20], in particular for Ni/Fe-based catalysts [14], although the real active site of Ni/Fe-based catalysts is still in debate [21]. For example, FRIEBEL et al [22] found that Fe^{3+} cations in

Corresponding author: Ye-jun LI, Tel: +86-731-88830857, E-mail: yejunli@csu.edu.cn;
Wei-hong QI, Tel: +86-29-88495240, E-mail: qiwh216@nwpu.edu.cn
DOI: 10.1016/S1003-6326(22)66077-1

γ-$Ni_{1-x}Fe_xOOH$ exhibit a lower overpotential than Ni^{3+} cations in either γ-$Ni_{1-x}Fe_xOOH$ or γ-NiOOH, which means that Fe^{3+} is the active site. However, LI et al [23] proposed that the doping of Fe^{3+} promoted the formation of Ni^{4+}, which in turn directly correlated to the enhanced OER performance. Despite of these, there is no doubt that the strong synergistic effect between Ni and Fe will contribute to the enhanced OER activity. In addition, it is noted that the metal phosphates can be converted to the metal (oxy)hydroxide through anion exchange in alkaline conditions [24], and many studies have demonstrated that the morphology and structure of metal phosphates can be varied with the change of phosphate precursors [25]. Therefore, the phosphate precursors (e.g., Na_3PO_4, Na_2HPO_4 and NaH_2PO_4) may also have profound effects on the morphology and structure of the metal (oxy)hydroxides and thus their OER activity; however, they remain rather unexplored.

To address these challenges, we prepared Fe-based phosphate precatalysts on Ni foams (NF) using various phosphate precursors (Na_3PO_4, Na_2HPO_4 and NaH_2PO_4) via a facile co-precipitation approach and evaluated their OER performance in alkaline conditions. Our structural analysis indicates that the iron phosphates-based precatalysts will spontaneously convert into nickel−iron (oxy)hydroxides ($NiFeO_xH_y$) as the final catalysts under electrochemical activation process (cyclic voltammetry (CV) scans) in alkaline conditions, which exhibits different morphologies with the change of phosphate precursors. To be specific, the final catalysts synthesized with Na_2HPO_4 prefer to form two-dimensional nanosheets, while these with Na_3PO_4 and NaH_2PO_4 mainly consist of aggregated nanoparticles with some dispersed nanosheets. The resulting $NiFeO_xH_y$ nanosheets synthesized with Na_2HPO_4 possess a flower-like morphology with rich active sites, allowing facial contact of solution, fast release of the produced gaseous molecules, and effective electron transfer, which thus provides more active sites and high efficiency for the reaction with a remarkably high and durable OER activity.

2 Experimental

2.1 Chemicals

Potassium hydroxide (95% KOH, Aladdin), ethanol absolute (CH_3CH_2OH, Sinopharm), iron nitrate nonahydrate ($Fe(NO_3)_3·9H_2O$, Aladdin), sodium phosphate, tribasic, anhydrous (Na_3PO_4, Aladdin), disodium hydrogen phosphate dodecahydrate ($Na_2HPO_4·12H_2O$, Sinopharm), sodium dihydrogen phosphate dihydrate ($NaH_2PO_4·2H_2O$, Sinopharm), Ni foam (NF, 99.9% Ni, thickness 1.5 mm, Kunshan Metal Material Tech, Suzhou, China), carbon cloth (W0S1011, thickness 0.36 mm, CeTech Co., Ltd), and highly purified water (> 18 MΩ·cm resistivity) were used. Before using, Ni foams were sonicated in 1 mol/L HCl for 0.5 h and washed in purified water.

2.2 Synthesis of $NiFeO_xH_y$/NF

$NiFeO_xH_y$/NF was synthesized through a facile co-precipitation and electrochemical activation strategy. Firstly, 0.025 mmol $Fe(NO_3)_3·9H_2O$ and 0.025 mmol $Na_2HPO_4·12H_2O$ were dissolved in 100 μL water. Later, 50 μL alcohol was added and the mixture was sonicated for 0.5 h to get a light-yellow mixture. The precursors were dropped onto Ni foams (10 mm × 10 mm × 1.5 mm) and dried at room temperature for 1 h as the precatalysts, which were directly used as electrodes. Subsequently, $NiFeO_xH_y$ nanosheets will be constructed spontaneously on the NF during the CV activation process, which is named as $NiFeO_xH_y$/NF-1H. Similarly, $NiFeO_xH_y$/NF-0H and $NiFeO_xH_y$/NF-2H were synthesized via the substitution of $Na_2HPO_4·12H_2O$ with Na_3PO_4 and $NaH_2PO_4·2H_2O$, respectively.

2.3 Characterization

Transmission electron microscopy (TEM) and high-resolution transmission electron microscope (HRTEM) were carried out by JEOL JEM 2100 microscope. The morphology and elemental composition of the synthesized catalysts were characterized by scanning electron microscopy (SEM, TESCAN MIRA3) equipped with energy-dispersive X-ray (EDS). X-ray diffraction (XRD) measurements were carried out on D/max 2550 VB equipped with Cu K_α radiation of 1.5418 Å. X-ray photoelectron spectroscopy (XPS) spectra were measured on Thermo ESCALAB 250XI system. Raman spectra were obtained on Horiba Scientific LabRAM HR Evolution with the excitation laser of 532 nm. The pH values were tested by PHS−25.

2.4 Electrochemical measurements

Electrochemical measurements were conducted using a CHI 760E electrochemical analyzer/workstation (CH Instruments Inc. Austin) in 1 mol/L KOH (pH=13.8) at room temperature. A conventional three-electrode system was used, with Hg/HgO electrode as the reference electrode, a graphite rod (*d*6 mm) as the counter electrode, and the as-prepared catalysts as the working electrode. All samples were stabilized by 50 CV cycles before measurements. Linear sweep voltammetry (LSV) measurements were IR-compensated (90%) and measured at a scan rate of 5 mV/s. All the potentials were calibrated with respect to a reversible hydrogen electrode (RHE) via φ(RHE)=φ(Hg/HgO)+0.059pH+φ_0(Hg/HgO). The electrochemical double layer capacitance (C_{dl}) was tested in 1 mol/L KOH solution with CV scanning from 1.04 to 1.14 V (vs RHE). Electrochemical impedance spectroscopy (EIS) measurements were carried out in the frequency range of 0.1 Hz to 100 kHz at an overpotential of 205 mV.

3 Results and discussion

The schematic illustration of the fabrication process is depicted in Fig. 1(a). The mixed solutions were prepared via dissolving $Fe(NO_3)_3{\cdot}9H_2O$ and the relative phosphate precursors (Na_3PO_4, $Na_2HPO_4{\cdot}12H_2O$, or $NaH_2PO_4{\cdot}2H_2O$) in water−alcohol solutions. The varying color of mixtures with different phosphate precursors was observed under visual inspection, suggesting the formation of iron phosphates. The obtained mixtures were then dropped on Ni foams as precatalysts and dried in vacuum oven at 60 °C. The precatalysts were then directly used as the electrodes in alkaline electrolyte to form the metal (oxy)hydroxide as the final catalysts via electrochemical activation process. The conversion progress of the precatalysts of $NiFeO_xH_y$/NF-1H via electrochemical activation is demonstrated in Fig. 1(b). Generally, it can be stabilized after around 50 CV cycles with a scan rate of 50 mV/s, indicating the accomplishment of conversion of the precatalysts.

3.1 Crystal structure of pre- and final-catalysts

To verify the crystal structures of the pre-catalysts and final-catalysts, XRD analysis was carried out (Fig. 2). However, all the precatalysts with different phosphate precursors only show three pronounced sharp peaks at 44.5°, 51.8° and 76.4°, corresponding to the (110), (200) and (220) planes of the fcc nickel, respectively, while no clear diffraction patterns can be found for both metal phosphates and metal oxyhydroxides, which can be attributed to the amorphous nature of the metal phosphates and the low contents of both on the Ni foams [26].

The morphologies of pre- and final-catalysts of $NiFeO_xH_y$/NF-0H, $NiFeO_xH_y$/NF-1H, and $NiFeO_xH_y$/NF-2H are shown in Fig. 3. Surprisingly, although no obvious change can be found for $NiFeO_xH_y$/NF-0H (Figs. 3(a) and (d)) and $NiFeO_xH_y$/NF-2H (Figs. 3(c) and (f)) after the electrochemical activation (aggregated nanoparticles with a small amount of fragmentized nanosheets), $NiFeO_xH_y$/NF-1H (Figs. 3(b) and (e)) clearly shows a flower-like morphology with rich nanosheets, indicating that Na_2HPO_4 can engender

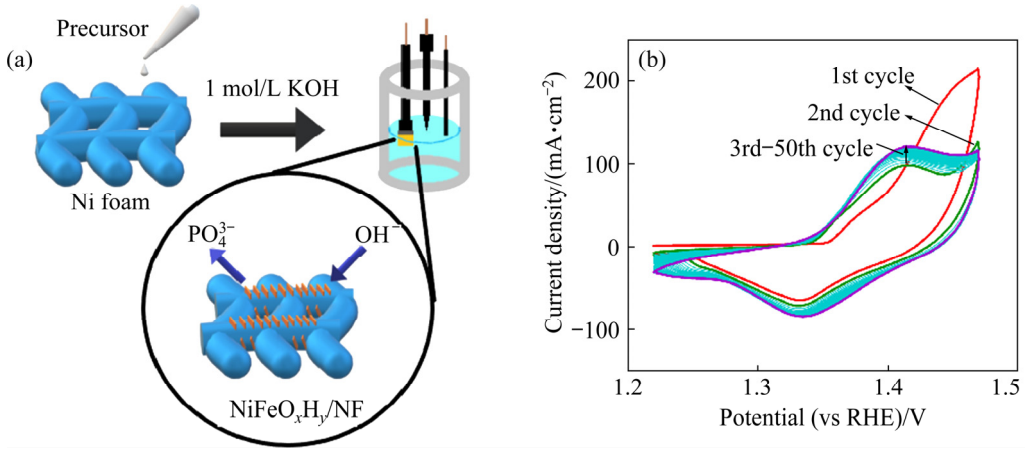

Fig. 1 Illustration of fabrication process of $NiFeO_xH_y$/NF (a) and electrochemical activation process of precatalysts of $NiFeO_xH_y$/NF-1H via CV activation in alkaline condition (b)

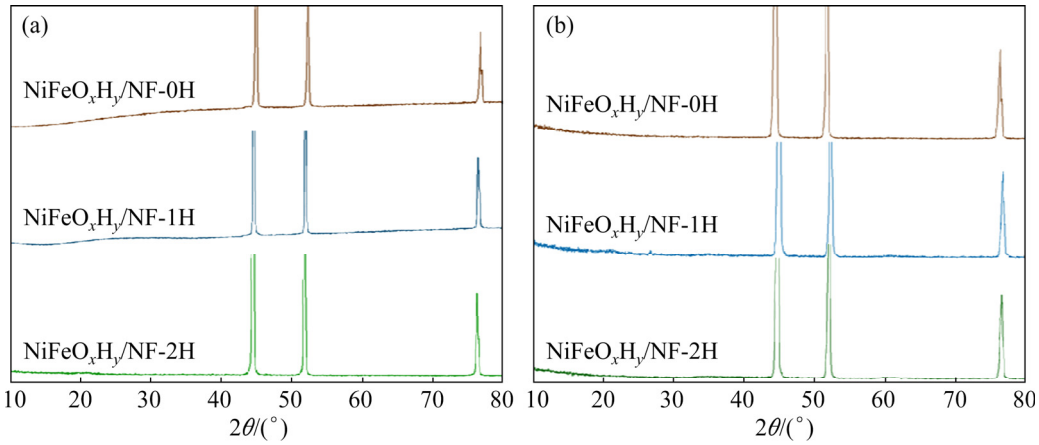

Fig. 2 XRD patterns of pre-catalysts (a) and final-catalysts (b) of NiFeO$_x$H$_y$/NF-0H, NiFeO$_x$H$_y$/NF-1H and NiFeO$_x$H$_y$/NF-2H

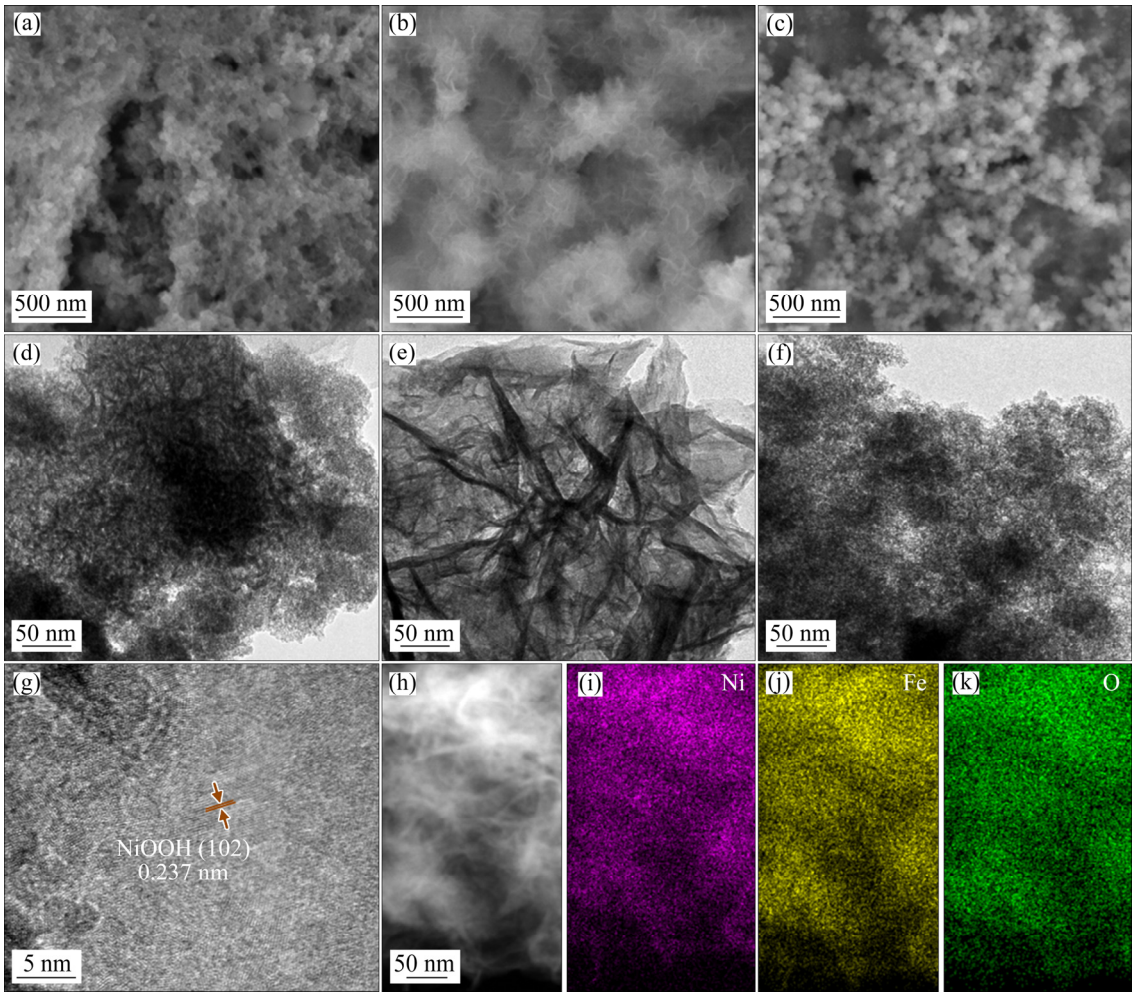

Fig. 3 SEM (a, b, c) and TEM (d, e, f) images of final catalysts of NiFeO$_x$H$_y$/NF-0H (a, d), NiFeO$_x$H$_y$/NF-1H (b, e) and NiFeO$_x$H$_y$/NF-2H (c, f), HRTEM (g) and HADDF (h) images of NiFeO$_x$H$_y$/NF-1H, and corresponding elemental mapping images of Ni (i), Fe (j) and O (k)

the most appropriate state of the precatalysts for the formation of metal (oxy)hydroxide nanosheets. This is confirmed by a lattice fringe of 0.237 nm via HRTEM, corresponding to the (102) plane of NiOOH. In addition, we applied elemental mapping to analyze composition of the catalysts, which

suggests uniform distributions of Fe, Ni and O. It is interesting to note that Ni appears in the formed metal (oxy)hydroxide nanosheets, indicating slightly dissolving of Ni from the Ni foams during the electrochemical activation process. Moreover, EDS spectra demonstrate an abrupt drop of P content from 9.8% (precatalysts) to 0.3% (final catalysts) for $NiFeO_xH_y$/NF-1H, suggesting a quite complete conversion of metal phosphates to NiFe (oxy)hydroxides.

To further verify the surface chemical compositions and electronic structure of the obtained catalysts, XPS was conducted. The full XPS spectra of the final catalysts of $NiFeO_xH_y$/NF-0H, $NiFeO_xH_y$/NF-1H and $NiFeO_xH_y$/NF-2H indicate the existence of Ni, Fe and O in the catalysts (see Fig. 4(a)), where no P peaks can be found, in line with EDS results, further confirming the conversion of Fe phosphates to NiFe (oxy)hydroxides. Figures 4(b−d) show the high-resolution XPS spectra of O 2p, Ni 2p and Fe 2p, respectively. As shown in Fig. 4(b), the O 1s spectra show strong peaks at ~530.5 eV, corresponding to the O 1s in a hydroxide-like (M—OH) environment, i.e. NiFe (oxy)hydroxide [6,27−30]. The higher shoulder around 532 eV can be attributed to oxygen in the absorbed water molecules [31], while the lower shoulder around 528 eV is defined as the lattice oxygen in oxide environment (M—O) due to the formation of oxyhydroxides [30,32]. Ni 2p spectra in Fig. 4(c) exhibit binding energies (BEs) centered at ~854 and ~872 eV with two shakeup satellites at ~860 and ~878 eV, which can be attributed to Ni $2p_{3/2}$ and Ni $2p_{1/2}$ of Ni^{2+}, respectively [33,34], due to the surface oxidation of Ni in the air. More importantly, BEs centered at ~856 and ~874 eV can be assigned to Ni^{3+} in NiOOH [35]. XPS spectra of Fe 2p show main BEs at ~713 and ~727 eV, which can be assigned to Fe $2p_{3/2}$ and Fe $2p_{1/2}$ of FeOOH, respectively [36,37]. The BEs at ~711 and ~724 eV for Fe $2p_{3/2}$ and Fe $2p_{1/2}$ of $Fe(OH)_3$ suggest the exchanges of PO_4^{3-} with OH^-, which leads to the further conversion during activation [38,39].

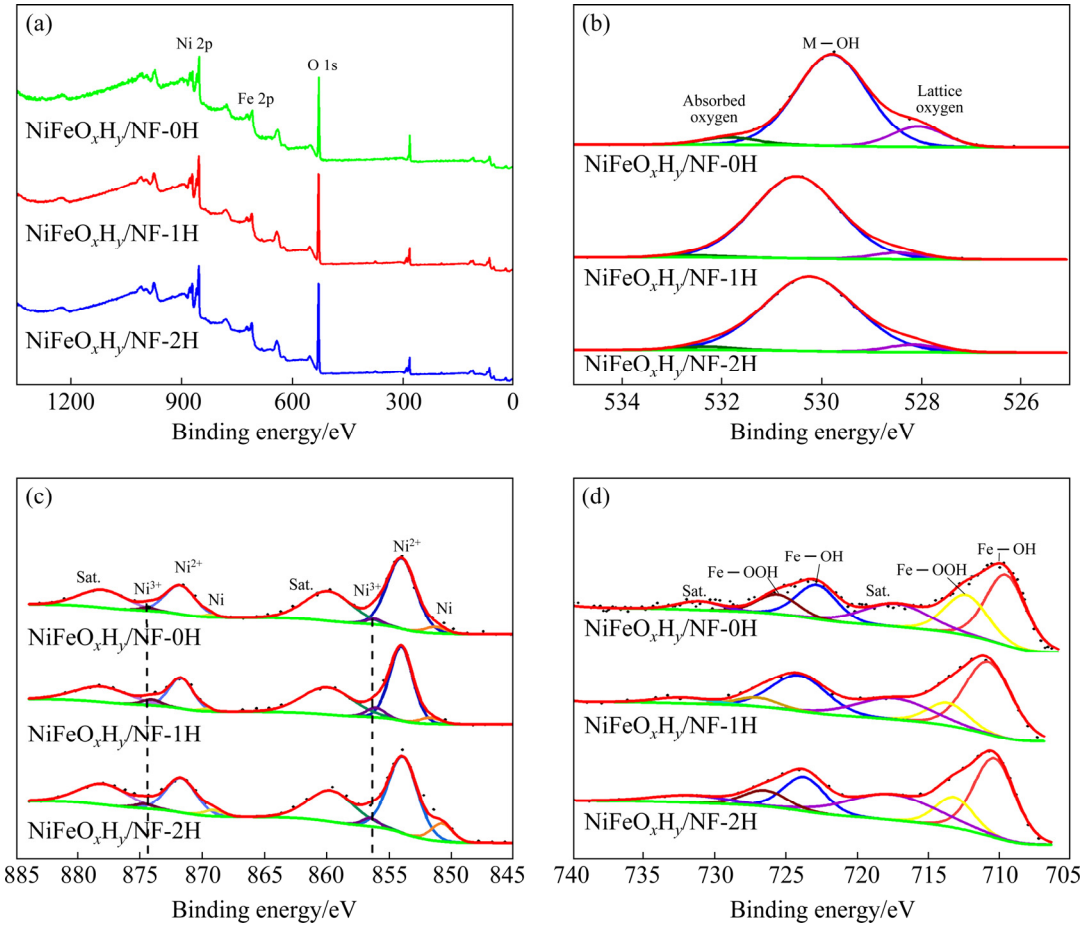

Fig. 4 XPS spectra of survey scan (a), O 1s (b), Ni 2p (c) and Fe 2p (d) of final catalysts of $NiFeO_xH_y$/NF-0H, $NiFeO_xH_y$/NF-1H and $NiFeO_xH_y$/NF-2H

3.2 Electrochemical properties of catalysts

The OER activities of the final catalysts of $NiFeO_xH_y$/NF-0H, $NiFeO_xH_y$/NF-1H, and $NiFeO_xH_y$/NF-2H were evaluated in 1 mol/L KOH by linear sweep voltammetry (LSV), as shown in Fig. 5(a). $NiFeO_xH_y$/NF-1H exhibited a much higher OER activity than $NiFeO_xH_y$/NF-0H and $NiFeO_xH_y$/NF-2H. It only requires an overpotential of 205 mV to generate current density of 50 mA/cm^2, which is much lower than those of $NiFeO_xH_y$/NF-0H (225 mV) and $NiFeO_xH_y$/NF-2H (243 mV). The fast OER catalytic kinetics of $NiFeO_xH_y$/NF-1H was further confirmed by the low Tafel slope of 30 mV/dec, compared to the other two samples (Fig. 5(b)). More importantly, $NiFeO_xH_y$/NF-1H can rank among the most active catalysts reported

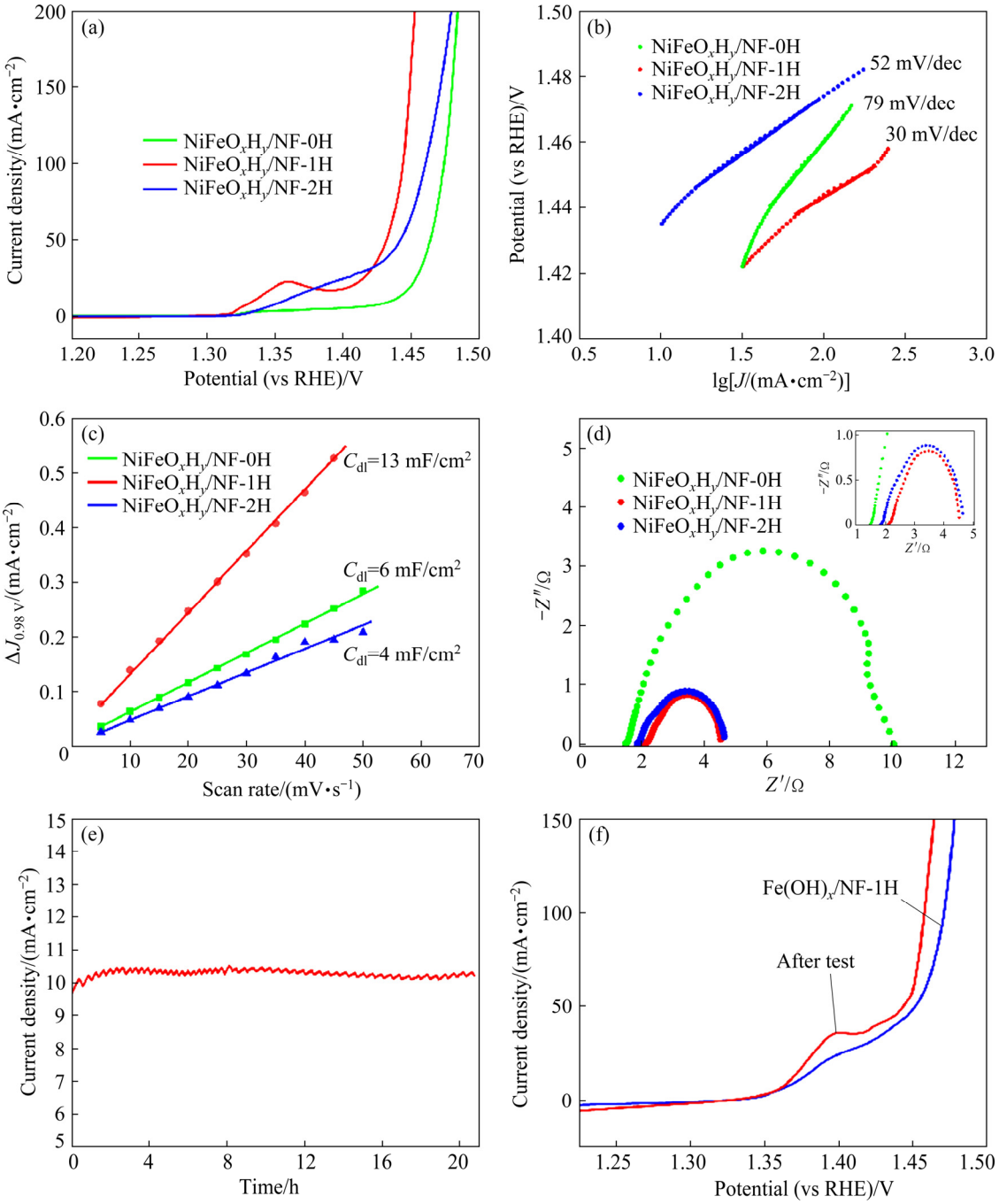

Fig. 5 LSV curves (a), Tafel plots (b), capacitive currents as function of scan rate (c) and Nyquist plots (overpotential=205 mV) (d) of final catalysts of $NiFeO_xH_y$/NF-0H, $NiFeO_xH_y$/NF-1H and $NiFeO_xH_y$/NF-2H, long-term stability test at 1.42 V (vs RHE) of $NiFeO_xH_y$/NF-1H (e), and LSV curves of $NiFeO_xH_y$/NF-1H before and after stability test (f)

recently. To explain the difference among activities, more electrochemical measurements were carried out. Activities are universally acknowledged to be closely related to surface area which is predicted to determine the double-layer capacitance (C_{dl}). As shown in Fig. 5(c), C_{dl} of the as-prepared catalysts is consistent with the OER activities, with an order of $NiFeO_xH_y$/NF-1H > $NiFeO_xH_y$/NF-0H > $NiFeO_xH_y$/NF-2H. The larger surface area of $NiFeO_xH_y$/NF-1H can be ascribed to the optimal structures of (oxy)hydroxide nanosheets, which can provide a tremendous amount of active sites. In addition, the presented electrochemical impedance spectroscopy (EIS) plots in Fig. 5(d) reveal a lower resistance of $NiFeO_xH_y$/NF-1H than those of the other two samples, due to the flower-like morphology with high conductivity of catalysts. The high OER activity of $NiFeO_xH_y$/NF-1H can therefore be attributed to its optimal nanosheets structures with a flower-like morphology, providing more active sites and high efficiency for the reaction and allowing the facial contact of solution, fast release of the produced gaseous molecules, and high conductivity. Additional measurement was carried out to confirm the formation of NiFe (oxy)hydroxide than pure Fe (oxy)hydroxide on the Ni foams. As shown in Fig. 6, the 1H catalysts on carbon cloths show much lower OER activity than that on Ni foams. This is because the 1H catalysts on carbon cloths are mainly composed of Fe-based (oxy)hydroxides with the low electrical conductivity. The present results suggest that the Fe phosphate under CV activation in alkaline condition can result in leaching of Ni from the NF, thus forming NiFe (oxy)hydroxides.

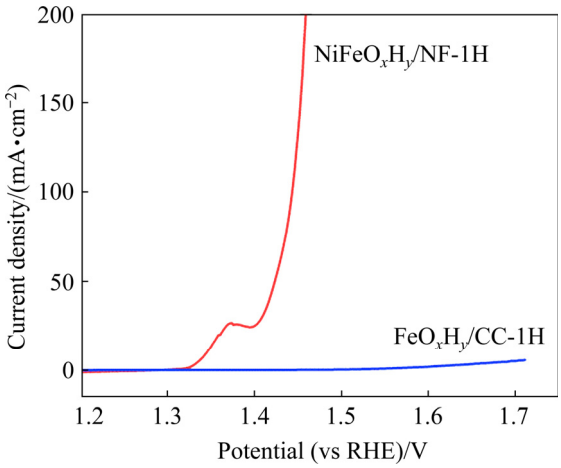

Fig. 6 Comparison of OER activity of 1H catalysts on Ni foam and carbon cloths

Aside from the activity, the stability of the catalysts is rather crucial for practical applications. Figure 5(e) shows J–t curve at 1.42 V (vs RHE) of $NiFeO_xH_y$/NF-1H for 20 h with stable current density, indicating good stability. Moreover, LSV curves of $NiFeO_xH_y$/NF-1H before and after stability test only showed a small change (14 mV) of the overpotential at 50 mA/cm^2 (Fig. 5(f)), further confirming its good long-term stability. XPS and SEM were also conducted to verify the electronic state and morphology of the catalysts after stability test. As shown in Figs. 7(a) and (b), high-resolution XPS spectra of Fe 2p indicate the core doublet at 724.3 and 710.0 eV assigned to Fe^{3+}, while O 1s spectrum shows negligible changes with the strong peak at 530.2 eV, indicating that $NiFeO_xH_y$ was stable after stability test [40]. Moreover, the nanosheets structures of $NiFeO_xH_y$/NF-1H were largely retained after test (Fig. 7(c)), confirming its good stability.

3.3 Mechanism of diverse effects of precursors

Based on the current observations, it is demonstrated that the various precursors (Na_3PO_4, Na_2HPO_4 and NaH_2PO_4) have different effects on the structure, morphology, and thus the activity of the final catalysts. We tentatively attribute these to the pH dependent effects. Na_3PO_4 can provide a more alkaline environment (pH=12.5) with excessive OH^-, which may induce the slight formation of $NiFeO_xH_y$ on the surface before the reconstruction via CV cycles. This may then block the formation of layered $NiFeO_xH_y$ nanosheets during the reconstruction process. On the contrary, the slightly acidic condition provided by $H_2PO_4^-$ (pH=3.6) may also restrain the formation of layered $NiFeO_xH_y$ nanosheets during the CV cycles. To verify the pH dependent effect, a sample was synthesized with iron nitrate and KOH as precursors (pH=13.4), named as $NiFeO_xH_y$/NF-KOH. Similarly, the mixed precursor was dropped onto Ni foams and dried in vacuum as the precatalysts. Later, the final catalysts were obtained with 50 CV scans in 1 mol/L KOH. It is strongly aggregated as shown by the SEM image (Fig. 8). This can be ascribed to the certain amount of $NiFeO_xH_y$ formed during the mixing of iron nitrate and KOH, which then limits the formation of nanosheets and only results in a significant aggregation of NiFe (oxy)hydroxides during CV

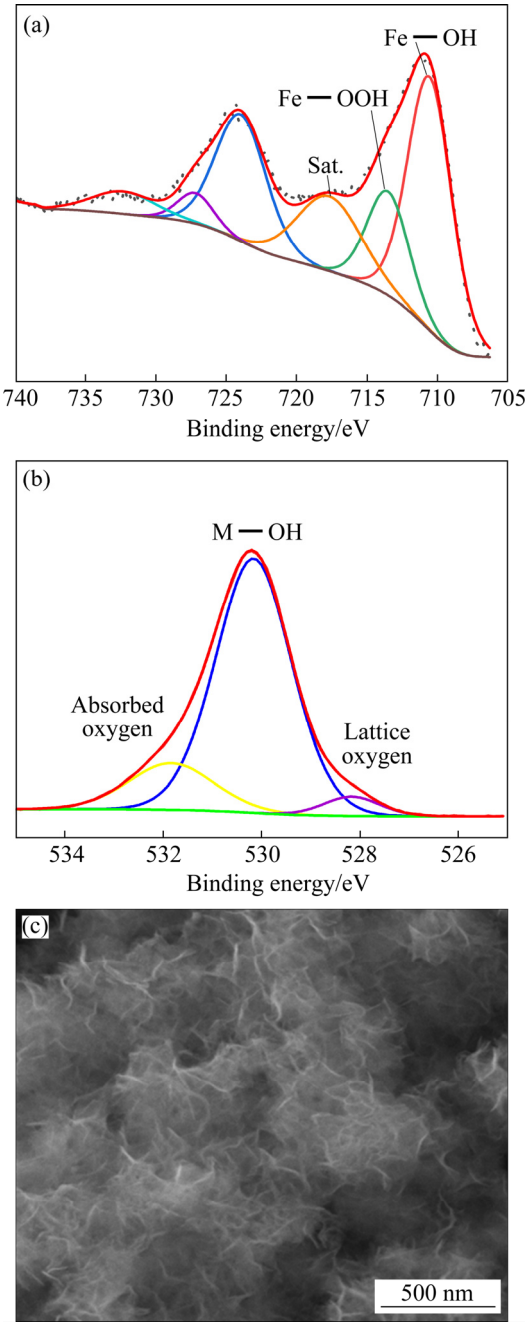

Fig. 7 High-resolution XPS spectra of Fe 2p (a) and O 1s (b) of $NiFeO_xH_y$/NF-1H after stability test, and SEM image of $NiFeO_xH_y$/NF-1H after stability test (c)

scans. Therefore, a moderate pH value (9.8) induced by Na_2HPO_4 is critical for formation of nanosheets during the reconstruction process.

3.4 Effects of experiment conditions

Additional experiments were carried out to explore the effect of experimental conditions on the performance of the catalysts. To find the ideal solvent (water and alcohol) for the precursors, three different molar ratios of water to alcohol were tested. Pure alcohol as solvent was avoided because ionization is unable to proceed without water. As shown in Fig. 9(a), the samples fabricated by pure water exhibit the poorest OER activity, because

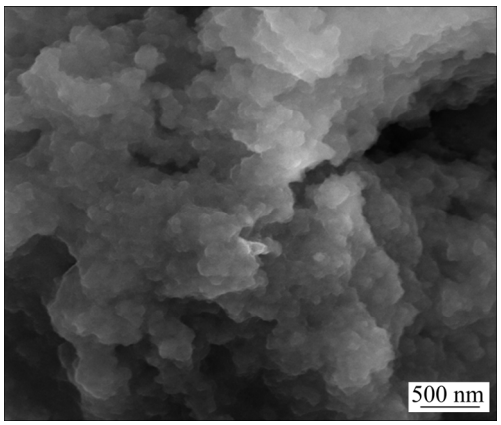

Fig. 8 SEM image of $NiFeO_xH_y$/NF-KOH

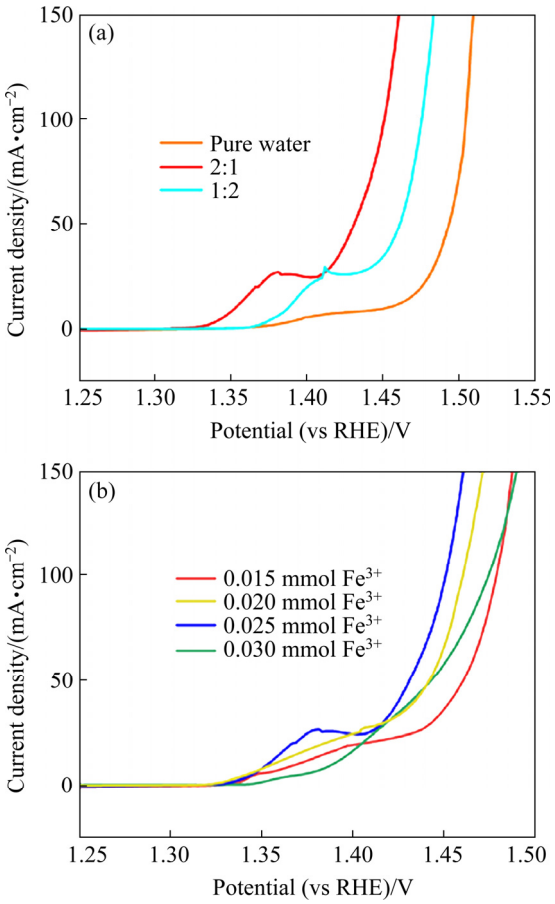

Fig. 9 LSV curves of $NiFeO_xH_y$/NF-1H synthesized from precursors with molar ratio of water to alcohol=1:0 (pure water), 2:1 and 1:2 as solvent (a), and $NiFeO_xH_y$/NF-1H with different loading amounts of Fe^{3+} (0.015, 0.02, 0.025, and 0.03 mmol) on Ni foam (b) (The as-prepared $NiFeO_xH_y$/NF-1H in our work was obtained from precursors with molar ratio of water to alcohol= 2:1 and 0.025 mmol Fe^{3+})

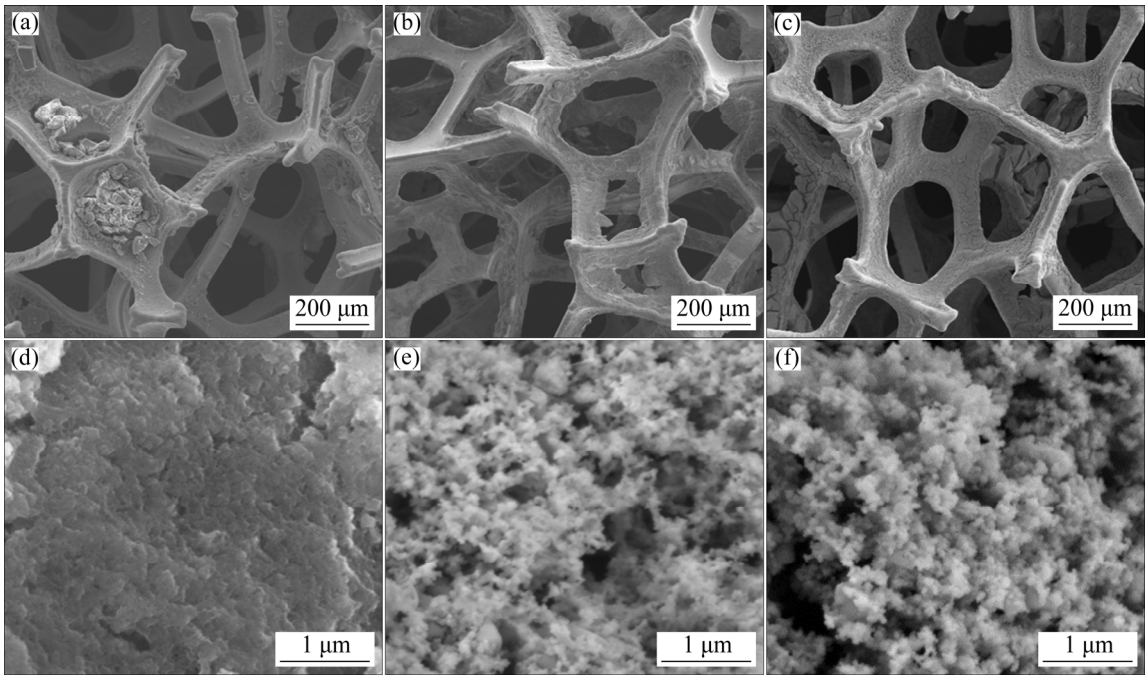

Fig. 10 SEM images of $NiFeO_xH_y$/NF-1H synthesized from precursors with water to alcohol molar ratio of 1:0 (pure water): (a, d) 2:1; (b, e) 1:2; (c, f) As-solvent

alcohol can enhance the dispersion of precursors on Ni foam, which can effectively reduce the agglomeration thus provide more sites for the growth and formation of $NiFeO_xH_y$ nanosheets. This result can be demonstrated by SEM images of the precursors with different ratios of water to alcohol. As shown in Fig. 10, the precursors with pure water are agglomerated on Ni foam, while those with alcohol and water are uniformly distributed on Ni foam. Therefore, a proper ratio of solvent (2:1) can be beneficial to the growth of (oxy)hydroxide nanosheets, thus enhancing activities of the as-prepared catalysts. It is universally acknowledged that loading mass is unable to be overlooked while designing the catalysts. The increase of the amount of catalysts may significantly affect the performance of catalysts. The LSV curves in Fig. 9(b) reveal the enhanced performances with the increase of loading amount of Fe^{3+}, where excessive catalysts on Ni foam will only reduce the OER activity, probably due to the overgrowth of NiFe (oxy)hydroxides.

4 Conclusions

(1) A series of pre catalysts with different phosphate precursors on Ni foam were successfully synthesized via co-precipitation, which were transformed into NiFe (oxy)hydroxide during electrochemical activation in alkaline electrolytes.

(2) Different phosphate precursors have diverse effects on the morphology and performances of catalysts after electrochemical activation, due to different environments and morphologies caused by the precursors.

(3) The final catalysts with Na_2HPO_4 ($NiFeO_xH_y$/NF-1H) have a morphology of nanosheets to provide a tremendous amount of active sites, which thus displays outstanding electrochemical activity (an overpotential of 205 mV at 50 mA/cm^2), low Tafel plot (30 mV/dec) and high durability.

Acknowledgments

This work was supported by the National Natural Science Foundation of China (Nos. 11904411, 52072308), and the Fundamental Research Funds for the Central Universities, China (Nos. 3102021MS0404, 3102019JC001).

References

[1] ROGER I, SHIPMAN M A, SYMES M D. Earth-abundant catalysts for electrochemical and photoelectrochemical water

splitting [J]. Nature Reviews Chemistry, 2017, 1(1): 0003.

[2] LI Ye-jun, PEI Wei, HE Jie-ting, LIU Kang, QI Wei-hong, GAO Xiao-hui, ZHOU Si, XIE Hai-peng, YIN Kai, GAO Yong-li, HE Jun, ZHAO Ji-jun, HU Jun-hua, CHAN Ting-shan, LI Zhou, ZHANG Gu-fei, LIU Min. Hybrids of PtRu nanoclusters and black phosphorus nanosheets for highly efficient alkaline hydrogen evolution reaction [J]. ACS Catalysis, 2019, 9(12): 10870−10875.

[3] YANG Peng, JIA chen, JIANG Liang-xing, WANG Tian-yi, YANG Hai-chao, LIU Fang-yang, MING Jia. Preparation of Sb_2O_3/Sb_2S_3/FeOOH composite photoanodes for enhanced photoelectrochemical water oxidation [J]. Transactions of Nonferrous Metals Society of China, 2020, 30(6): 1625−1634.

[4] CHEN Ya-qiong, ZHANG Jin-feng, LEI Wan, HU Wen-bin, LEI Liu, ZHONG Cheng, DENG Yi-da. Effect of nickel phosphide nanoparticles crystallization on hydrogen evolution reaction catalytic performance [J]. Transactions of Nonferrous Metals Society of China, 2017, 27(2): 369−376.

[5] BAI L C, HSU C S, ALEXANDER D T L, CHEN H M, HU X. A cobalt-iron double-atom catalyst for the oxygen evolution reaction [J]. Journal of the American Chemical Society, 2019, 141(36): 14190−14199.

[6] BURKE M S, KAST M G, TROTOCHAUD L, SMITH A M, BOETTCHER S W. Cobalt−iron (oxy)hydroxide oxygen evolution electrocatalysts: The role of structure and composition on activity, stability, and mechanism [J]. Journal of the American Chemical Society, 2015, 137(10): 3638−3648.

[7] TAHIR M, PAN L, IDREES F, ZHANG Xiang-wen, WANG Li, ZOU Ji-jun, WANG Zhong-lin. Electrocatalytic oxygen evolution reaction for energy conversion and storage: A comprehensive review [J]. Nano Energy, 2017, 37: 136−157.

[8] LI Yan-juan, MIN Wang, SA Liu, GAO Jing-xia, SHUN Yang, LIU Zi-hao, LAI Xiao-yong, XIAO Yan. Preparation and properties of transition metal nitrides caged in N-doped hollow porous carbon sphere for oxygen reduction reaction [J]. Transactions of Nonferrous Metals Society of China, 2021, 31(5): 1427−1438.

[9] WANG Yan, CHEN Ze-hua, HUANG Jing, LI Gao-jie, CAO Jian-liang, ZHANG Bo, CHEN Xing-ying, ZHANG Huo-li, JIA Lei. Preparation and catalytic behavior of reduced graphene oxide supported cobalt oxide hybrid nanocatalysts for CO oxidation [J]. Transactions of Nonferrous Metals Society of China, 2018, 28(11): 2265−2273.

[10] LI Ye-jun, ZHOU Xin-feng, QI Wei-hong, XIE Hai-peng, YIN Kai, TONG Yong-gang, HE Jun, GONG Shen, LI Zhou. Ultrafast fabrication of Cu oxide micro/nano-structures via laser ablation to promote oxygen evolution reaction [J]. Chemical Engineering Journal, 2020, 383: 123086.

[11] WU Hao-fei, YIN Kai, QI Wei-hong, ZHOU Xin-feng, HE Jie-ting, LI Jin-ming, LIU Yan-yu, HE Jun, GONG Shen, LI Ye-jun. Rapid fabrication of Ni/NiO@CoFe layered double hydroxide hierarchical nanostructures by femtosecond laser ablation and electrodeposition for efficient overall water splitting [J]. Chem Sus Chem, 2019, 12(12): 2773−2779.

[12] DUAN Ran, LI Ye-jun, GONG Shen, TONG Yong-gang, LI Zhou, QI Wei-hong. Hierarchical CoFe oxyhydroxides nanosheets and Co2P nanoparticles grown on Ni foam for overall water splitting [J]. Electrochimica Acta, 2020, 360: 136994.

[13] MA Wei, MA Ren-zhi, WU Jing-hua, SUN Peng-zhan, LIU Xiao-he, ZHOU Ke-chao, SASAKI T. Development of efficient electrocatalysts via molecular hybridization of NiMn layered double hydroxide nanosheets and graphene [J]. Nanoscale, 2016, 8(19): 10425−10432.

[14] GUO Rong-hui, LAI Xiao-xu, HUANG Jian-wen, DU Xin-chuan, YAN Yi-chao, SUN Ying-hui, ZOU Gui-fu, XIONG Jie. Phosphate-based electrocatalysts for water splitting: Recent progress [J]. Chem Electro Chem, 2018, 5(24): 3822−3834.

[15] TROTOCHAUD L, YOUNG S L, RANNEY J K, BOETTCHER S W. Nickel−iron oxyhydroxide oxygen-evolution electrocatalysts: The role of intentional and incidental iron incorporation [J]. Journal of the American Chemical Society, 2014, 136(18): 6744−6753.

[16] SUN Hua-chuan, LI Jian-Gang, LV Lin, LI Zhi-shan, AO Xiang, XU Chen-hui, XUE Xin-ying, HONG Guo, WANG Chun-dong. Engineering hierarchical CoSe/NiFe layered-double-hydroxide nanoarrays as high efficient bifunctional electrocatalyst for overall water splitting [J]. Journal of Power Sources, 2019, 425: 138−146.

[17] SHIN H, XIAO Hai, GODDARD W A. In silico discovery of new dopants for Fe-doped Ni oxyhydroxide ($Ni_{1-x}Fe_xOOH$) catalysts for oxygen evolution reaction [J]. Journal of the American Chemical Society, 2018, 140(22): 6745−6748.

[18] LI Jian-Gang, SUN Hua-chuan, LV Lin, LI Zhi-shan, AO Xiang, XU Chen-hui, LI Yi, WANG Chun-dong. Metal−organic framework-derived hierarchical (Co,Ni)Se_2@NiFe LDH hollow nanocages for enhanced oxygen evolution [J]. ACS Applied Materials & Interfaces, 2019, 11(8): 8106−8114.

[19] CUI Yan, XUE Yuan, ZHANG Rui, ZHANG Jian, LI Xing-ao, ZHU Xin-bao. Vanadium–cobalt oxyhydroxide shows ultralow overpotential for the oxygen evolution reaction [J]. Journal of Materials Chemistry A, 2019, 7(38): 21911−21917.

[20] YI Ling-ya, NIU Yan-li, FENG Bo-min, ZHAO Ming, HU Wei-hua. Simultaneous phase transformation and doping via a unique photochemical–electrochemical strategy to achieve a highly active Fe-doped Ni oxyhydroxide oxygen evolution catalyst [J]. Journal of Materials Chemistry A, 2021, 9(7): 4213−4220.

[21] ANANTHARAJ S, KUNDU S, NODA S. “The Fe effect”: A review unveiling the critical roles of Fe in enhancing OER activity of Ni and Co based catalysts [J]. Nano Energy, 2021, 80: 105514.

[22] FRIEBEL D, LOUIE M W, BAJDICH M, SANWALD K E, CAI Y, WISE A M, CHENG M J, SOKARAS D, WENG T C, ALONSO-MORI R, DAVIS R C, BARGAR J R, NØRSKOV J K, NILSSON A, BELL A T. Identification of highly active Fe sites in (Ni,Fe)OOH for electrocatalytic

water splitting [J]. Journal of the American Chemical Society, 2015, 137(3): 1305−1313.

[23] LI N, BEDIAKO D K, HADT R G, HAYES D, KEMPA T J, VON CUBE F, BELL D C, CHEN L X, NOCERA D G. Influence of iron doping on tetravalent nickel content in catalytic oxygen evolving films [J]. Proceedings of the National Academy of Sciences of the United States of America, 2017, 114(7): 1486−1491.

[24] LIU Xin-he, YIN Quan-zhou, DAI Chen-chen, LI Guo-chun, LIAN Jia-biao, ZHAO Yan, YANG Shi-liu, LI Hua-ming. Amorphous bimetallic phosphate–carbon precatalyst with deep self-reconstruction toward efficient oxygen evolution reaction and Zn–air batteries [J]. ACS Sustainable Chemistry & Engineering, 2021, 9(15): 5345−5355.

[25] LI Hai-yan, YU Hong-wen, ZHAI Jia-li, SUN Lei, YANG Hong-jun, XIE Song-hai. Self-assembled 3D cobalt phosphate octahydrate architecture for supercapacitor electrodes [J]. Materials Letters, 2015, 152: 25−28.

[26] ZOU Xu, LIU Yi-pu, LI Guo-dong, WU Yuan-yuan, LIU Da-peng, LI Wang, LI Hai-wen, WANG De-jun, ZHANG Yu, ZOU Xiao-xin. Ultrafast formation of amorphous bimetallic hydroxide films on 3D conductive sulfide nanoarrays for large-current-density oxygen evolution electrocatalysis [J]. Advanced Materials, 2017, 29(22): 1700404.

[27] HE Wen-jun, REN Gang, LI Ying, JIA Dong-bo, LI Shi-yun, CHENG Jia-ning, LIU Cai-chi, HAO Qiu-yan, ZHANG Jun, LIU Hui. Amorphous nickel–iron hydroxide films on nickel sulfide nanoparticles for the oxygen evolution reaction [J]. Catalysis Science & Technology, 2020, 10(6): 1708−1713.

[28] LIU Jiang, ZHOU Jia, LIU Shuang, CHEN Gui, WU Wei, LI Ying, JIN Pu-jun, XU Chun-li. Amorphous NiFe-layered double hydroxides nanosheets for oxygen evolution reaction [J]. Electrochimica Acta, 2020, 356: 136827.

[29] LIU Wei, LIU Hu, DANG Lian-na, ZHANG Hong-xiu, WU Xiao-lin, YANG Bin, LI Zhong-jian, ZHANG Xing-wang, LEI Le-cheng, JIN Song. Amorphous cobalt–iron hydroxide nanosheet electrocatalyst for efficient electrochemical and photo-electrochemical oxygen evolution [J]. Advanced Functional Materials, 2017, 27(14): 1603904.

[30] GUO Zhen-guo, YE Wen, FANG Xiao-yu, WAN Jian, YE Yao-yao, DONG Ying-ying, CAO Ding, YAN Dong-peng. Amorphous cobalt–iron hydroxides as high-efficiency oxygen-evolution catalysts based on a facile electrospinning process [J]. Inorganic Chemistry Frontiers, 2019, 6(3): 687−693.

[31] MORALES-GUIO C G, LIARDET L, HU Xi-le. Oxidatively electrodeposited thin-film transition metal (Oxy)hydroxides as oxygen evolution catalysts [J]. Journal of the American Chemical Society, 2016, 138(28): 8946−8957.

[32] XIAO Jun-wu, OLIVEIRA A M, WANG Lan, ZHAO Yun, WANG Teng, WANG Jun-hua, SETZLER B P, YAN Yu-shan. Water-fed hydroxide exchange membrane electrolyzer enabled by a fluoride-incorporated nickel–iron oxyhydroxide oxygen evolution electrode [J]. ACS Catalysis, 2021, 11(1): 264−270.

[33] JIANG Jing, ZHANG Cai-hong, AI Lun-hong. Hierarchical iron nickel oxide architectures derived from metal-organic frameworks as efficient electrocatalysts for oxygen evolution reaction [J]. Electrochimica Acta, 2016, 208: 17−24.

[34] ZHAO Jin-xiu, REN Xiang, HAN Qing-zhi, FAN Da-wei, SUN Xu, KUANG Xuan, WEI Qin, WU Dan. Ultra-thin wrinkled NiOOH−$NiCr_2O_4$ nanosheets on Ni foam: An advanced catalytic electrode for oxygen evolution reaction [J]. Chemical Communications, 2018, 54(39): 4987−4990.

[35] YANG Huan, GONG Lan-qian, WANG Hong-ming, DONG Chung-li, WANG Jun-lei, QI Kai, LIU Hong-fang, GUO Xing-peng, XIA Bao-yu. Preparation of nickel-iron hydroxides by microorganism corrosion for efficient oxygen evolution [J]. Nature Communications, 2020, 11(1): 5075.

[36] XU Hui, WEI Jing-jing, LIU Chao-fan, ZHANG Yang-ping, TIAN Lin, WANG Cai-qin, DU Yu-kou. Phosphorus-doped cobalt−iron oxyhydroxide with unltrafine nanosheet structure enable efficient oxygen evolution electrocatalysis [J]. Journal of Colloid and Interface Science, 2018, 530: 146−153.

[37] ZHOU Qian, CHEN Ya-ping, ZHAO Guo-qiang, LIN Yue, YU Zhen-wei, XU Xun, WANG Xiao-lin, LIU Hua Kun, SUN Wen-ping, DOU Shi-xue. Active-site-enriched iron-doped nickel/cobalt hydroxide nanosheets for enhanced oxygen evolution reaction [J]. ACS Catalysis, 2018, 8(6): 5382−5390.

[38] YAN Feng, ZHU Chun-ling, LI Chun-yan, ZHANG Shen, ZHANG Xi-tian, CHEN Yu-jin. Highly stable three-dimensional nickel–iron oxyhydroxide catalysts for oxygen evolution reaction at high current densities [J]. Electrochimica Acta, 2017, 245: 770−779.

[39] SIAL M A Z G, BASKARAN S, JALIL A, TALIB S H, LIN Hai-feng, YAO Yue-chao, ZHANG Qi, QIAN Hai-xia, ZOU Ji-zhao, ZENG Xie-rong. NiCoFe oxide amorphous nanohetrostructures for oxygen evolution reaction [J]. International Journal of Hydrogen Energy, 2019, 44(41): 22991−23001.

[40] ZHOU Min, WENG Qun-hong, ZHANG Xiu-yun, WANG Xi, XUE Yan-ming, ZENG Xiang-hua, BANDO Y, GOLBERG D. In situ electrochemical formation of core–shell nickel–iron disulfide and oxyhydroxide heterostructured catalysts for a stable oxygen evolution reaction and the associated mechanisms [J]. Journal of Materials Chemistry A, 2017, 5(9): 4335−4342.

磷酸盐前驱体对泡沫镍上生长的镍/铁羟基氢氧化物形貌及析氧反应性能的影响

段 然[1,2]，李业军[1,2]，王 舒[1]，仝永刚[3]，Horst-Günter RUBAHN[4]，张固非[4]，齐卫宏[5]

1. 中南大学 物理与电子学院 纳米光子学与器件湖南省重点实验室，长沙 410083；
2. 中南大学 材料科学与工程学院，长沙 410083；
3. 长沙理工大学 汽车与机械工程学院，长沙 410076；
4. NanoSYD, Mads Clausen Institute and DIAS Danish Institute for Advanced Study, University of Southern Denmark, Alsion 2, DK-6400 Sonderborg, Denmark;
5. 西北工业大学 凝固技术国家重点实验室 先进润滑与密封材料研究中心，西安 710072

摘 要：通过共沉积法和电化学激活法在泡沫镍网上生长制备镍/铁羟基氢氧化物纳米片。研究发现，不同磷酸盐前驱体(Na_3PO_4、Na_2HPO_4 和 NaH_2PO_4)对最终催化剂的形貌及析氧反应活性有不同的影响。使用 Na_2HPO_4 制备的镍/铁羟基氢氧氯化物纳米片在 1 mol/L KOH 溶液中电流密度达到 50 mA/cm^2 时所需过电位为 205 mV，Tafel 斜率低至 30 mV/dec，并可以在后续稳定性测试中保持稳定 20 h。

关键词：镍/铁羟基氧化物；铁基磷酸盐；析氧反应；电化学激活

(Edited by Xiang-qun LI)